

①

AD-A220 520

FILE COPY

LABORATORY OF PLASMA STUDIES

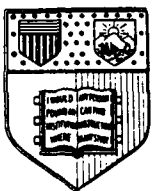
Ion Beam Propagation in a Solenoidal Magnetic Field

J.J. Moschella, R. Kraft, and B.R. Kusse

Laboratory of Plasma Studies
Cornell University
Ithaca, New York 14853

LPS 340

October 1984



DTIC
ELECTED
APR 13 1990
S E D
CO

CORNELL UNIVERSITY
ITHACA, NEW YORK

DISTRIBUTION STATEMENT A
Approved for public release; Distribution Unlimited

90 04 12 158

I. Introduction

An experimental study of an intense space charge neutralized ion beam propagating into a solenoidal magnetic field is presented. The data shows that the observed focusing effects are adequately described by a theory for beam propagation proposed by S. Robertson [1,2]. In an experiment conducted by Robertson, a similar beam was focused by a short magnetic field where the focal point was outside the field region. This experiment shows that the same theory can be used to describe a beam which comes to a focus within the uniform region of the solenoid.

The theory essentially states that ions undergo single particle motion modified by the beam neutralizing electrons which produces focal distances much shorter than ions acting alone. The physics of this type of focusing is similar to a lens system originally investigated by D. Gabor [5]. In the Gabor lens, electrons that prefill a magnetic mirror produce electrostatic fields which assist in the focusing of a stream of ions. The Robertson theory, which is presented in Section II, assumes a cylindrically symmetric beam which does not significantly perturb the magnetic field, maintenance of local space charge neutrality and perfectly cold neutralizing electrons. The discussion which follows concerns itself with all these assumptions except the latter. The neglect of electron pressure effects appears to be valid based on theoretical studies of ion beams which are vacuum neutralized. The studies, by S. Humphries et al., show that ion beams can be brought to a focus with negligible limits imposed by electron pressure [3,4]. An expression for the minimum spot size that was determined predicts a minimum radius which is at

least an order of magnitude smaller than that observed in this experiment. Clearly, in such a situation, the aberrations discussed in Section III B are the limiting factor in determining the minimum beam radius. Also in Section III a model is presented for a theoretical determination of the focal distance as a function of field strength. In Section IV the experimental procedure is discussed and data presented.

II. Theory

A. Basic Equations

In the Robertson theory single particle trajectories of electrons and ions are modified by a local electric field which maintains spacial charge neutrality. In addition, the applied magnetic field is assumed unperturbed by the beam. That is, $\delta B/B \ll 1$, where δB are the self fields of the beam and B is the magnetic field formed by the current carrying coils. Furthermore, the theory assumes that the proton beam has cylindrical symmetry. Under these conditions spacial charge neutrality will require the same radial and axial motions of electrons and ions.

An equation to describe this collective motion can be obtained by imposing the neutrality condition on the single particle motions of electrons and ions. Formally we can write the Lagrangian for a single particle of mass m_α and charge q_α as follows:

$$L = \frac{1}{2} m_\alpha (\vec{V}_\alpha)^2 + q_\alpha \vec{V}_\alpha \cdot \vec{A} - q_\alpha \phi \quad (1)$$

where \vec{V} is the particle velocity, \vec{A} is the magnetic vector potential formed by applied currents and ϕ is the electrostatic potential. By the symmetry of the fields and the beam nothing depends on the coordinate ϕ and A has only a ϕ component, therefore the beam conserves canonical angular momentum. If the beam enters the magnetic field from a field free region with no rotation then

$$\dot{\phi} = \frac{q_\alpha A_\phi}{m_\alpha r_\alpha} \quad (2)$$

which becomes $\dot{\phi} = \pm \frac{1}{2} \Omega_\alpha$ in the uniform field region of the solenoid; Ω_α is the cyclotron frequency of the α species. By using equation (2) we can express the radial equation as

$$\ddot{r}_\alpha(t) = \left(\frac{q_\alpha}{m_\alpha}\right)^2 A_\phi \frac{\partial A_\phi}{\partial r} - \frac{q_\alpha}{m_\alpha} E_r . \quad (3)$$

To satisfy the neutrality condition we require that $r_i(t) = r_e(t)$, by solving equation (3) for $\alpha=i$ and $\alpha=e$ simultaneously we obtain:

$$\ddot{r}(t) = - \frac{e^2}{m_i m_e} A_\phi \frac{\partial A_\phi}{\partial r} \quad (4)$$

$$E_r = \frac{e}{m_i m_e} [m_e - m_i] A_\phi \frac{\partial A_\phi}{\partial r} \quad (5)$$

where in equation (4) $r(t)$ is now the radial position of both ions and electrons. It is important to note that equation (4) is exactly the same as a single particle equation for a pseudoparticle with a charge-to-mass ratio of $e/\sqrt{m_i m_e}$. Therefore, the effect of this collective interaction on beam propagation is to replace each electron-ion pair with such a pseudoparticle.

The same process can be performed for the motion equations in the z -direction to obtain:

$$\ddot{z}(t) = - \frac{e^2}{m_i m_e} A_\phi \frac{\partial A_\phi}{\partial z} \quad (6)$$

$$E_z = \frac{e}{m_i m_e} [m_e - m_i] A_\phi \frac{\partial A_\phi}{\partial z}. \quad (7)$$

The numerical integration of these equations has shown that equation (6) represents a small correction to the motion that would otherwise be obtained by assuming a constant axial velocity.

It should be noted that without a cylindrically symmetric beam equations (4) and (6) do not hold. This is easy to understand physically because the derived equations are based on conservation of canonical angular momentum. In the non symmetric case rotation of electrons in one direction and ions in the other will bring about electric fields in the ϕ direction. This destroys conservation of angular momentum and thus the entire analysis. In order to achieve results which agree with theory the beam should be as symmetric as possible.

B. Validity of Assumptions

The assumptions of an unperturbed field and local space charge neutrality can be put into a convenient form. The actual field considered in this experiment is a 61 cm solenoid with an 8 cm cusp. It is evident that the majority of the radial motion will take place while the beam is in the uniform field region where $A_\phi = rB_z/2$. This is verified by computer simulations which include the fringing field effects.

1. Neutrality. In the uniform field region we may rewrite equation (5) as

$$E_r = \frac{[m_e - m_i]}{4e} \Omega_i \Omega_e r . \quad (5a)$$

This is the only field component which exists in this region since $\partial A_\phi / \partial z = 0$ in equation (7). Using Gauss's Theorem and the above equation we obtain

$$\text{div}(E) = 4\pi e [n_i - n_e] = \frac{1}{2e} [m_e - m_i] \Omega_i \Omega_e \approx -\frac{m_e}{2e} (\Omega_e)^2$$

or

$$\frac{4\pi e^2}{m_e} [n_i - n_e] \approx -\frac{1}{2} (\Omega_e)^2 . \quad (8)$$

The space charge neutrality condition can be written as $|n_i - n_e| \ll n_e$; clearly upon examining equation (8) an equivalent condition may be expressed as

$$(w_{pe})^2 \gg \frac{1}{2} (\Omega_e)^2 \quad (9)$$

where w_{pe} is the electron plasma frequency.

2. Field Perturbations. Experimental data reflecting the beam's net current show that with magnetic fields of 1-3 kG the beam is 90% current neutralized. This results in an azimuthal field on the order of 10 Gauss or a 0.5% perturbation which is certainly negligible. However, the major source of field perturbation arises from the beam electrons which rotate as they enter the applied field producing fields in the z direction which oppose the applied field. The ions, due to their heavier mass do not contribute significantly to this azimuthal current. The current density which results from these rotating electrons is $J(r) = \frac{1}{2} e n_e r \Omega_e$ where equation (2) has been used. On axis the perturbed field is

$$|\delta B_z| = \frac{\mu_0 e n_e}{4} \Omega_e (R_b)^2 = \frac{B_z}{4} \left(\frac{w_{pe} R_b}{c} \right)^2 \quad (10)$$

where R_b is the radius of the beam. So for $|\delta B / B| \ll 1$ we have the equivalent condition

$$(R_b/2)^2 \ll (c/w_{pe})^2 . \quad (11)$$

This states that the magnetic skin depth must be greater than the beam radius.

Due to the density dependence of the inequalities through the electron plasma frequency, for a given magnetic field strength there may exist a density window where both inequalities can be satisfied. As the beam density increases the skin depth decreases and inequality (11) may be violated. For lower densities the neutrality condition may be violated. Therefore, for a given field strength equation (9) sets a lower limit on the beam density and equation (11) an upper limit. Table 1 lists the densities where the inequalities became equalities for fields of interest in this experiment (a 2 cm beam radius is assumed).

A typical beam density for this experiment is $1-2 \times 10^{11} \text{ cm}^{-3}$, which would indicate that good agreement with theory may be possible for field strengths below 1 kG. At higher field values the neutrality condition will be violated because the inertial response of the beam electrons is not fast enough to compensate for the charge separation induced by the magnetic field. It is then evident that the motion of beam electrons and ions will not lead to a common focus. The electrons will focus before the common focus point predicted by equations (4) and (6) and the ions after. This separation of focal points may be the cause of the "strange" charge collector signals observed for the large field values above 1 kG. Some of these signals are shown in Fig. 2. They are characterized by a large negatively directed spike. They consistently occur near the common focus point and are never observed farther down the tube. However, there is a large degree of shot-to-shot inconsistency with regard to the axial location of this feature.

III. Determination of Focal Point

Differential equations (4) and (6) can be time-integrated to obtain electron-ion trajectories for initial conditions of interest. The focal point is then determined by the axial position where a minimum in the beam radius occurs. This simulation was accomplished using a 4th order Runge-Kutta numerical calculation and a model for the magnetic field.

A. Field Model

The magnetic field is modeled by an infinitely thin current carrying cylinder having the same length, radius and number of ampere turns as the actual coils. (The real coils are 1/2-inch thick and separated by 1/2 inch.) The model coil current density is given by the following expression in cylindrical coordinates where $z=0$ is the center of the cylinder;

$$J_\phi(r', z') = \frac{NI}{L} \delta(r'-a) S(|z'| - \frac{1}{2}) \quad (12)$$

and NI - is the actual number of ampere turns

L - is the length of the solenoid (61 cm)

a - is the radius of the solenoid (10 cm)

S - is the unit step function.

Using the current density given above and performing the trivial r' integration, the magnetic vector potential becomes:

$$A_\phi(r, z) = \frac{\mu_0 NI}{4\pi L} \int_{-L/2}^{L/2} dz' \int_0^{2\pi} d\phi' \frac{\cos \phi'}{[(z-z')^2 + r^2 + a^2 - 2ra \cos \phi']^{1/2}}. \quad (13)$$

It is evident that for a beam with a radius less than 2 cm the square root in the denominator may be expanded as a power series in r/a . The ϕ' integration renders all terms even in r/a zero. The final results after all integrations is an odd power series in r/a .

$$A_\phi = \frac{\mu_0 NI}{4L} \left[\frac{z_+}{\beta_+^{1/2}} - \frac{z_-}{\beta_-^{1/2}} \right] \left[\frac{r}{a} \right] + \frac{3\mu_0 NI}{32L} \left[\frac{z_+}{\beta_+^{5/2}} - \frac{z_-}{\beta_-^{5/2}} \right] \left[\frac{r^3}{a^3} \right] + \dots \quad (14)$$

where $\beta_{\pm} \equiv z_{\pm}^2/a^2 + 1$ and $z_{\pm} \equiv z \pm L/2$.

Finally, we must take into account a conducting brass flange which exists 8 cm from the end of the solenoid. (See Fig. 1.) To model this aspect of the experiment a perfect cusp is created 8 cm from the end of the current carrying cylinder. This is accomplished quite simply by replacing the expression for the vector potential in equation (14) by the following combination:

$$\begin{aligned} A_\phi(r, z) &= A_\phi(r, L+2d-z) && \text{for } z > -(d+L/2) \\ A_\phi &= 0 && \text{for } z < -(d+L/2) \end{aligned} \quad (15)$$

and firing the test particles with a positive axial velocity originating where $A_\phi = 0$. (Note: d is the distance from the end of the cylinder to the cusp.)

B. Aberrations

The numerical integration of differential equations (4) and (6) using equation (15) and its derivatives is straightforward. The inclusion of the cubic term in A_ϕ and equation (6) accounts for spherical aberrations observed in the trajectories. Those particles launched at larger radii will

experience greater radial force than those launched nearer to the axis and as a result cross the z axis first. An example of these trajectories showing only spherical aberrations is given in Fig. 4, where test particles are launched at radii varying from 2 cm to .2 cm with an axial velocity of 76 cm/nsec. One can see that this effect is small and amounts to a smearing of the first focal point by less than 1/2 a centimeter. In this case the continuation of the trajectories past the first focal point show a well-defined second focus with only slightly more smearing.

A more serious form of aberration exists from a spread in the velocity distribution of ions in the beam. This is the analogue to chromatic aberrations observed in light optics. The velocity spread of the ions is assumed to originate in diode voltage variations which exist as the beam ions are extracted from the polyethylene anode. An estimate of these variations is 20% obtained from a typical diode voltage trace shown in Fig. 3. This produces a range in velocities of 68-84 cm/nsec. Figure 5 shows the effect when chromatic aberrations are added to the spherical aberrations. Once again test particles were launched at varying radii but at the velocity limits of 84 and 68 cm/nsec for each radius. One can see that the first focal point is smeared out over about 2 1/2 centimeters. The minimum radius is determined by the intersection of the outermost particle trajectories and is indicated in the figure. Table 2 shows values of the minimum radius and its location for field strengths of interest in this experiment.

It is interesting to note that the inclusion of chromatic aberration masks any second focal point which would exist for monoenergetic ions and electrons. This can be seen clearly in Figure 5 where the second focusing is

spread out axially over 6 cm. Where the 84 cm/nsec velocity components are focusing the 68 cm/nsec velocity components are almost completely defocused. The net result is that the beam will show only small density variations after the first focal point if the collective single particle motions are continued.

IV. Experimental Results

A. Apparatus

The apparatus used to take the data for this experiment is diagrammed in Figure 1. The beam is extracted from a planar magnetically insulated racetrack type diode. The diode was operated at 330 kV and was insulated at 2 times B-critical. The typical beam which is delivered has an ion current density of 10 A/cm^2 with an axial velocity of 76 cm/nsec for a 60 nanosecond pulse. Sources for beam neutralizing electrons are a slotted cathode and a grounded screen located at the beam port which leads to the pyrex drift tube. The bellows region between the port and drift tube contains two apertures which limit the beam radius to 2 cm; these apertures are separated axially by 18 cm. Approximately 8 cm from the bellows region is the first of a series of 24 equally spaced coils which form the focusing field. The coils have an inner radius of 10 cm, are 1/2-inch thick and are separated by 1/2-inch; the total length of the solenoid is 61 cm. The focusing field is formed by discharging a $200 \mu\text{F}$ capacitor circuit which is crowbared after the first peak to a slope of 5 amps/ μsec ; this corresponds to a field variation of 2×10^{-6} kG/nsec. The beam is fired at 85% of the peak coil current where the relationship between peak magnetic field and charging voltage is 1.05 kG/kV . The flange located at the opposite end of the pyrex tube contains a vacuum feed through so that the charge collectors may be varied axially to take data.

B. Data

Diagnostics for this experiment include diode voltage and current, Rogowski coils to measure net beam current and magnetic field current, heat sensitive thermalfax paper, charge collectors located on axis and 2 cm off axis. The charge collector used for the on axis measurements contained an array of nine holes, each 0.2 mm in diameter (see Fig. 6). The array of holes samples 0.28 mm^2 of beam area within a radius of 1.5 mm. The charge collector located off axis was a single hole type which sampled a beam area of 0.09 mm^2 . The collectors were set up so they could be moved axially or rotated while the system was under vacuum pressures. All data was taken at pressures between 1 and 3×10^{-5} Torr.

A Rogowski coil was positioned to measure the net beam current after propagation through the cusp region. These measurements indicated an increase in positive beam current when the magnetic field was on. This is presumably due to some electrons being turned around in the cusp region. However, even at field strengths near 3 kG the beam is still 90% current neutralized compared to 97% current neutralization observed with no magnetic field. Single particle electron trajectories show that only those electrons within a radius of .1 cm are not reflected at $B = 1 \text{ kG}$. Therefore, the majority of beam electrons are pulled through the cusp region by collective interaction with the ions.

The charge collector located 2 cm off axis and the thermalfax paper were used primarily to check the beam symmetry. It was found that the apertures which reduced the beam radius from 3.5 to 2 cm greatly increased the symmetry. This significantly improved the reproducibility of the data runs which was a severe problem before insertion of the apertures.

The focal point was determined experimentally by moving the charge collector axially and taking beam density measurements on axis. The density measurements reported indicate the average obtained over the pulse duration. Figure 2 shows a typical charge collector signal obtained near the focal point. For a given field strength the focal point is simply the axial position where a peak in the beam density is observed. To start a data run the probe was placed near the first field coil and systematically moved down the solenoid. While monitoring the diode I-V and field coil current, two shots were taken at each position to average out some of the shot-to-shot variations normally observed. Plots of the ion current density vs. axial position are shown in Figures 7 and 8 where each curve represents one data run. The plot obtained with no applied field reflects a beam divergence of about 4° . Data runs were taken to check these results and in every case the position of maximum beam density was the same. Once can see that at the focal point there is a density enhancement by as much as a factor of 6 compared to the density as the beam enters the field. The peak density corresponds to a decrease in the beam radius by a factor of 2.5 or a minimum radius of .8 cm. This is a rough estimate that assumes conservation of particles and maintenance of a square radial density profile. The smaller field strengths show a slightly lower peak value at the focal point. Table 2 lists for comparison the minimum radius inferred from the peak intensity measurement and that determined by methods discussed in Section II. This table shows that even with such a simplified calculation the trajectory plots give a ballpark value for the minimum beam radius.

Finally, a plot of the focal point position versus magnetic field strength is shown in Figure 9. The uncertainty bars indicate the accuracy in

determining the focal point for a single run. Also in Figure 9 is a curve reflecting the focal position predicted by the numerical calculation. Significant deviation from theory is observed for $B > 1$ kG where the predicted focal length is shorter than that observed. In view of the violation of inequality (9) this result need not be due to an inadequacy of the theory. The direction of the deviation from theory is consistent with the violation of charge neutrality since the ions have focused closer to their independent single particle focus. Nevertheless, the agreement at .6 kG, where the inequality is only marginally satisfied, is quite good.

As expected, no density enhancement after the first focus was ever observed. After focusing the beam density steadily decreased and then leveled off in every case. This observation may be due to velocity variations cited in Section III or to a more complicated form of defocusing not accounted for in this simple theory.

In conclusion, it appears that the focusing effects of an intense ion beam can be described by this simple theory with reasonable accuracy even though some of the assumptions have been violated. The continuation of the modified single particle trajectory past the first focal point remains an unanswered question. However, the data obtained past the first focus does not disprove this conjecture since the results can be explained by a finite velocity spread of ions in the beam.

References

- [1] S. Robertson, Phys. Rev. Let. 48, 149 (1982).
- [2] S. Robertson, Phys. Fluids 26, 1129 (1983).
- [3] S. Humphries, Jr., Appl. Phys. Let. 32, 792 (1978).
- [4] S. Humphries, Jr., T. R. Lockner, J. W. Poukey, J. P. Quintenz, Phys. Rev. Let. 46, 995 (1981).
- [5] S. Gabor, Nature 160, 90 (1947).

Table 1. Density limits of inequalities (9) and (11).

Maximum field (kG)	Lower limit for density (cm^{-3})	Upper limit for density (cm^{-3})
1	5×10^{10}	3×10^{11}
2	2×10^{11}	3×10^{11}
3	4.4×10^{11}	3×10^{11}

Table 2. Minimum radii for investigated field strengths.

Maximum field (kG)	Min. radius from trajectories (cm)	Min. radius from peak density (cm)
0.6	0.37	1.1
1.0	0.40	1.0
2.1	0.43	0.8
3.7	0.43	0.9

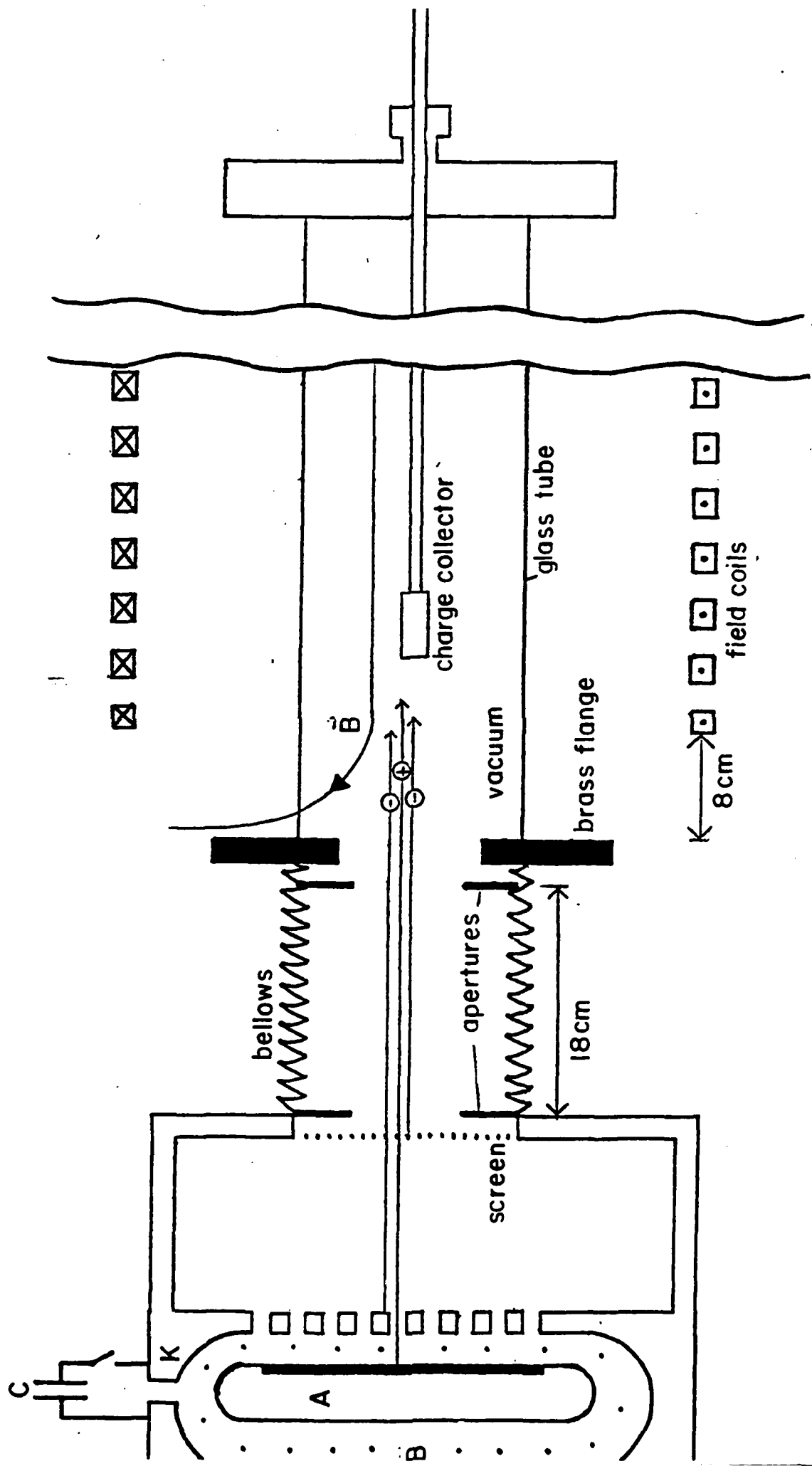


Figure 1: Apparatus. The aperture radius is 2 cm and the coil radius is 10 cm.

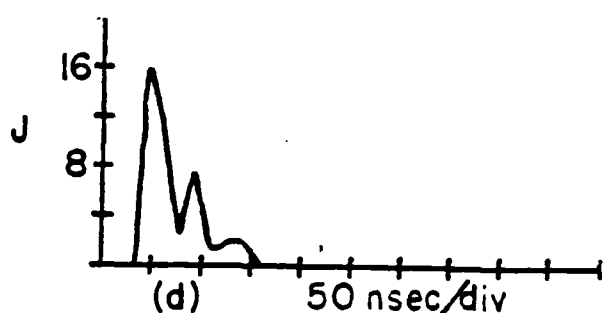
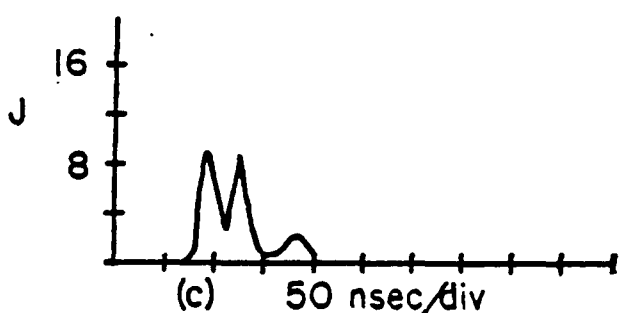
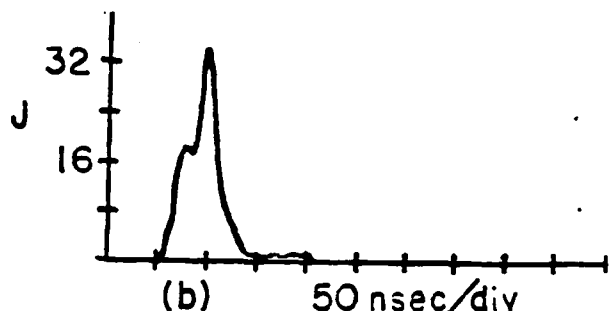
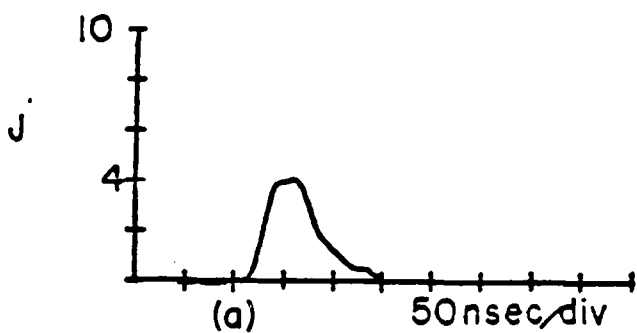


Figure 2: Oscilloscope traces of on axis charge collector signals where J is in A/cm^2 . (a) is a typical trace with $B=0$, (b) is a typical trace near the focal point, (c) & (d) are traces obtained at $z=11 \text{ cm}$ and $B=2.1 \text{ kG}$ showing the negative spiking behaviour.

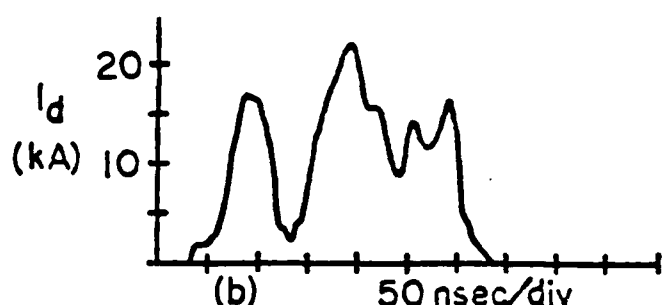
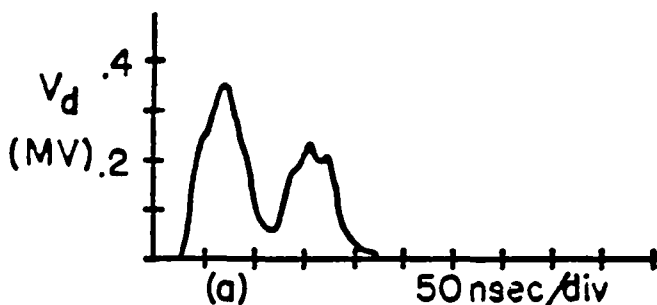


Figure 3: Oscilloscope traces of (a) the inductively corrected diode voltage and (b) the diode current.

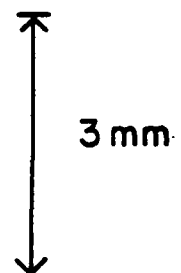


Figure 6: Hole array for the charge collector located on axis, each hole has a radius of .1 mm.

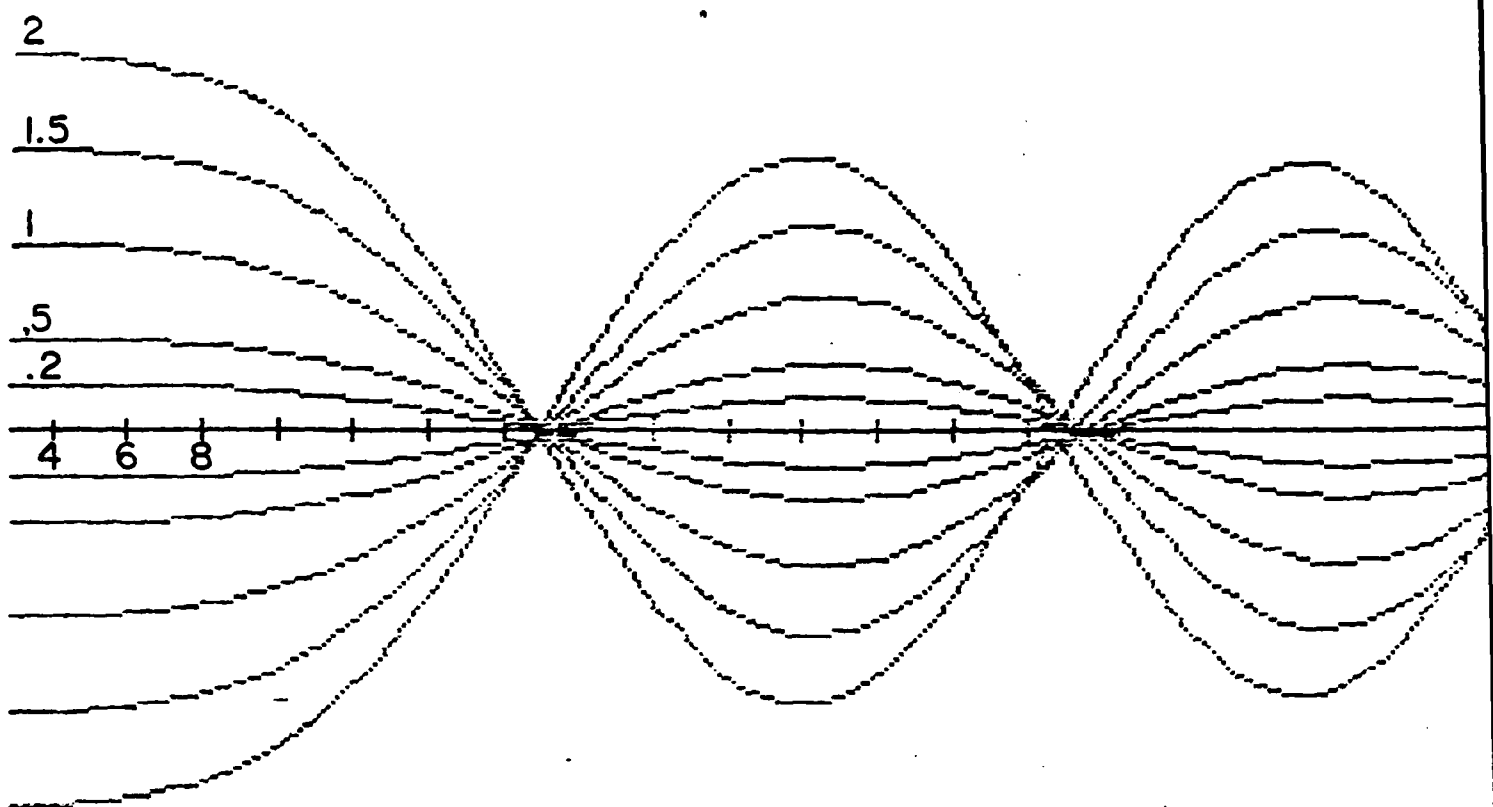


Figure 4: Trajectories for monoenergetic electrons and ions showing a well defined second focus. The radii and horizontal scale are indicated in centimeters for a field strength of 1 kG.

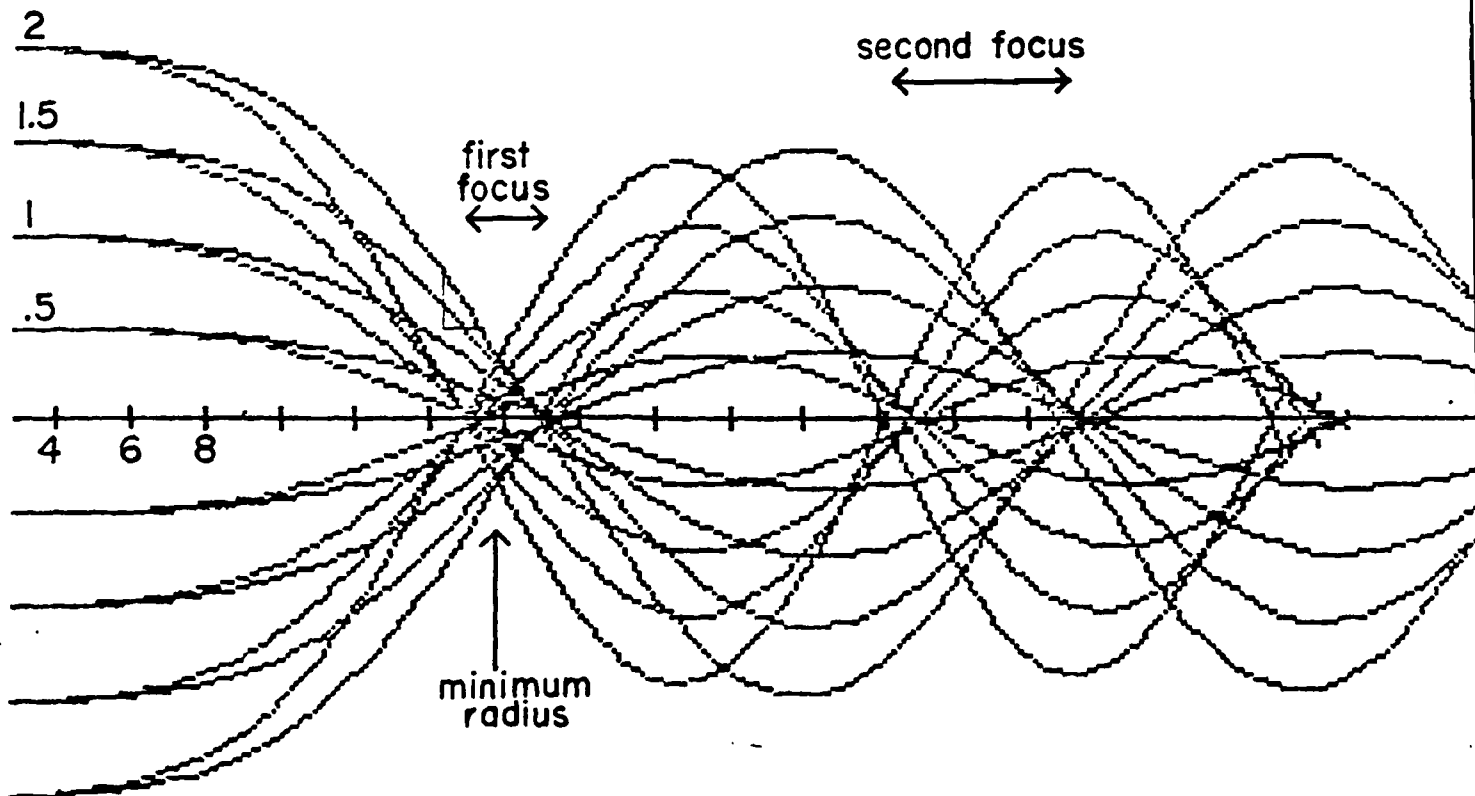


Figure 5: Electron-ion trajectories at the velocity limits of 84 and 68 cm/nsec showing extensive smearing of the second focus. The radii and horizontal scale are indicated in centimeters for a field strength of 1 kG.

$x - B = 2.1 \text{ kG}$
 $\Delta - B = 1.0 \text{ kG}$
 $o - B = 0$

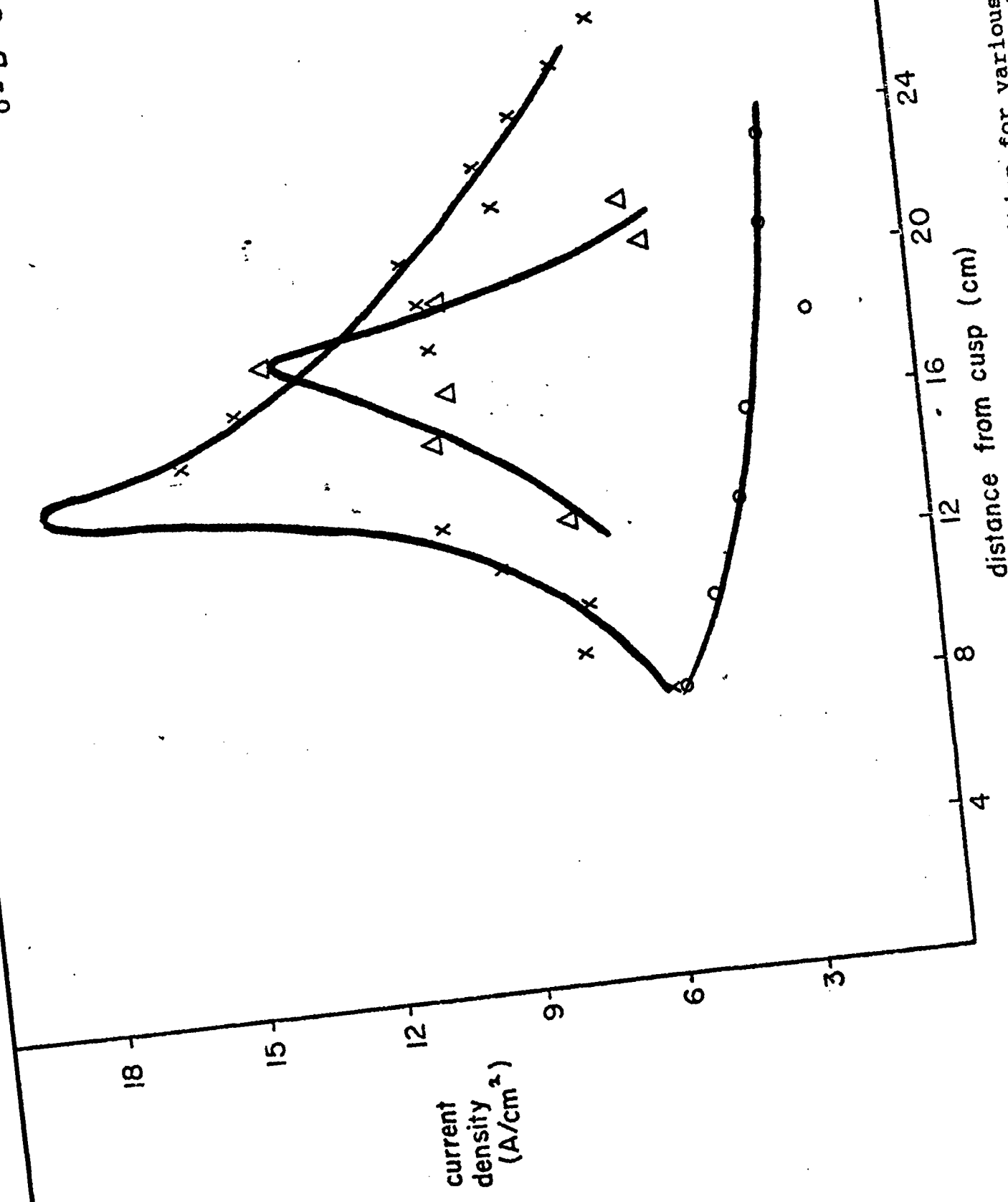


Figure 7: Ion current density on axis vs axial position for various field strengths. The density is averaged over the pulse duration.

$x - B = 3.7 \text{ kG}$
 $o - B = 1.5 \text{ kG}$
 $\Delta - B = 0.6 \text{ kG}$

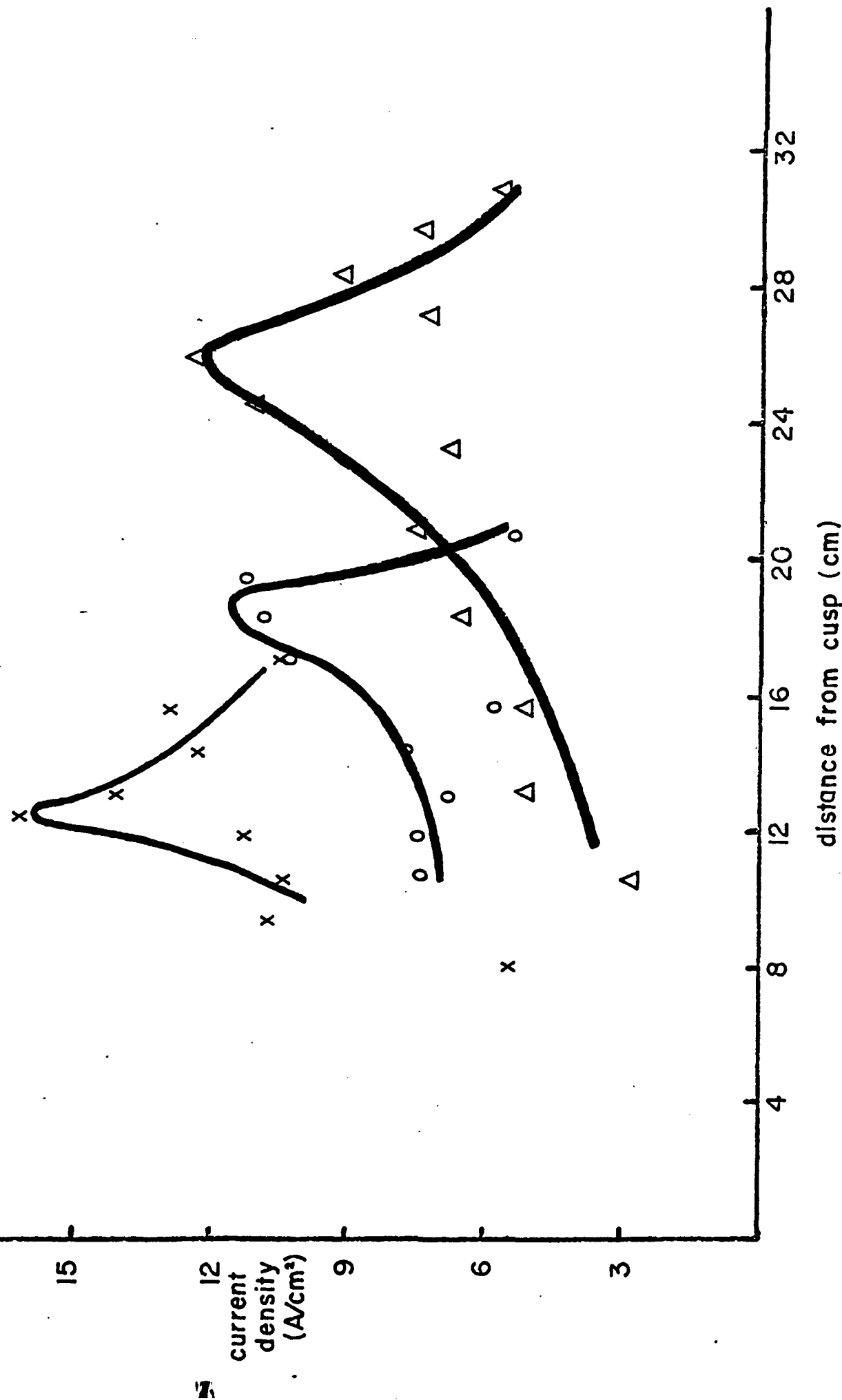


Figure 8: Ion current density on axis vs axial position for various field strengths. The density is averaged over the pulse duration.

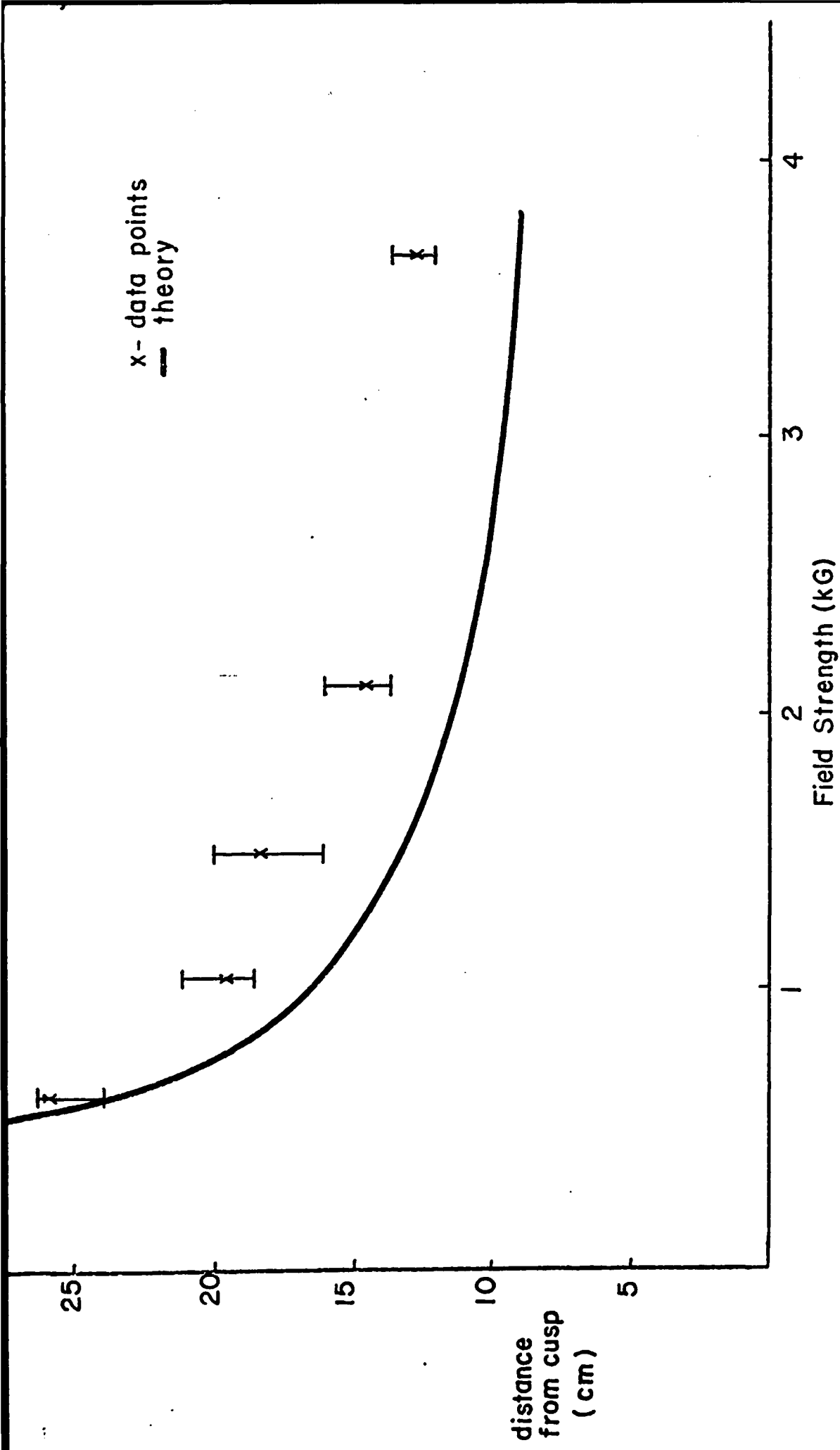


Figure 9: First focus location vs applied field strength. The uncertainty bars indicate the uncertainty in determining the focal position for a single run.